Applied Physics B (2023) 129:148
https://doi.org/10.1007/s00340-023-08092-x

Applied Physics B
Lasers and Optics

RESEARCH

Optical synthesis of soliton molecules using composite filtering effects in a fiber laser

Lin Gu[1] · Zhen Liu[1] · Yiqing Shu[1] · Jianqing Li[2] · Weicheng Chen[1]

Received: 22 June 2023 / Accepted: 23 August 2023 / Published online: 5 September 2023

Abstract
The manipulation of coherent multipulse generations is a promising ultrafast pulse technique. In this study, we experimentally obtain for the first time the synthesis of various soliton molecules (SMs) with different pulse spacings and phases based on composite filtering effects in a fiber laser. The composite filtering functions are constructed by multiplying the nonlinear–polarization–rotation (NPR)- and Lyot-based filtering effects to achieve four processes from the coexistence, incoherent interaction, and weakly coherent interaction of two pulses to the generation of an SM. Theoretical and experimental analyses demonstrate that the manipulation of synthesizing SMs is due to the composite filtering functions. Our research provides a novel method for the manipulation of SM generation in a noise-driven nonlinear dissipative system, which has significant applications in the fields of pulse coding and coherent pulse detection.

1 Introduction

Passively mode-locked fiber lasers (PMLFLs) containing gain, loss, nonlinearity, dispersion, saturable absorption, filtering, etc., are ideal platforms for revealing rich nonlinear dissipative pulse dynamics [1]. Many interesting nonlinear multipulsing phenomena, such as soliton rain [2], soliton bunching [3], soliton explosions [4] and SMs [5, 6], have been experimentally observed in PMLFLs. Among them, SMs as a coherent multisoliton pattern have attracted much attention in the field of nonlinear optics. SMs were first theoretically predicted by Malomed in nonlinear Schrödinger or Ginzburg–Landau equations [7] and then experimentally verified by Tang et al. in a passively mode-locked fiber laser [8]. Similar to a chemical molecule originating from the interaction balance among chemical bonds of atoms, an SM is a bound entity constructed by a set of solitons with a fixed phase difference under the coherent interactions among solitons [9, 10]. In contrast to higher order solitons, SMs are insensitive to external perturbations, which are beneficial for extended pulse coding in high-speed communication and ultrafast coherent pulse detection.

There are two types of coherent pulse interactions for forming SMs in bound states, i.e., long- and short-range interactions among solitons. Regarding long-range interactions in which the pulse spacing is far beyond a five-time pulse duration, the coherent interaction should be assisted by dispersive waves or continuous waves (CW) to generate a bound state [11]. On the other hand, short-range direct interactions originating from the overlapping of adjacent solitons [12, 13] can produce a tightly bound state. The coherent interaction of internal pulses in SMs could be experimentally observed through a real-time spectroscopy technique [6, 14]. Synthesizing or dissociating SMs is an interesting and important issue in nonlinear physics. The ordinary way to obtain SMs in a fiber laser is to adjust intracavity dispersion and nonlinear effects for modulating short-range direct interactions between pulses, which can construct various SMs with different pulse spacings [15]. However, the rule of SM generation does not monotonically depend on the dispersion and nonlinearity parameters, resulting in nonreproducible SM generation. Recently, on-demand SM generation has been manipulated to achieve by a parallel optical–soliton reactor [16]. Moreover, some physical effects, e.g., direct pump modulation [17] and dispersion loss [18], are also

✉ Yiqing Shu
shu.yq@fosu.edu.cn

✉ Weicheng Chen
chenwch@fosu.edu.cn

[1] Guangdong-Hong Kong-Macao Joint Laboratory for Intelligent Micro-Nano Optoelectronic Technology, School of Physics and Optoelectronic Engineering, Foshan University, Foshan 528000, China

[2] School of Computer Science and Engineering, Macau University of Science and Technology, Macau 999078, China

used to tailor an SM. These works provide valuable ideas for actively manipulating the generation and physical characteristics of SMs. However, these methods require extra complex devices, which significantly increase the complexity and cost of the lasers. In this paper, we propose a novel way to manipulate the interaction of dual-wavelength pulses for synthesizing SMs using composite filtering effects. The composite filtering effects are achieved by multiplying the Lyot- and NPR-based filtering effects. Meanwhile, we can dynamically modulate different pulse spacings and phases of SMs. Theoretical and experimental analyses further demonstrate that the manipulation of synthesizing SMs is due to composite filtering effects. Our work will provide an efficient method for generating various SMs and deepen the understanding of coherent pulse interactions in ultrafast lasers.

2 Experimental setup

Figure 1 exhibits the experimental setup of a ring PMLFL composed of Lyot- and NPR-based filtering. Assisted by the connection of a wavelength–division multiplexer (WDM), a segment of 4-m commercial Er-doped fiber (YOFC EDF1022) with a gain coefficient of 20.1 dB/m pumped by a 980-nm laser was used for signal laser generation. A segment of 200-m conventional single-mode fiber (SMF) in the cavity could effectively reduce the self-started mode-locking threshold. The NPR mechanism was achieved by the joint operation of two polarization controllers (PC3 and PC4) and one polarization-dependent isolator (PD-ISO) in the ring cavity, which took the roles of both a mode locker and a potential filter. In addition, the joint operation of a 0.25-m polarization-maintaining fiber (PMF) and two PCs (PC1 and PC2) constituted a Lyot filter, as shown in the dashed box in Fig. 1. It should be noted that the Lyot- and

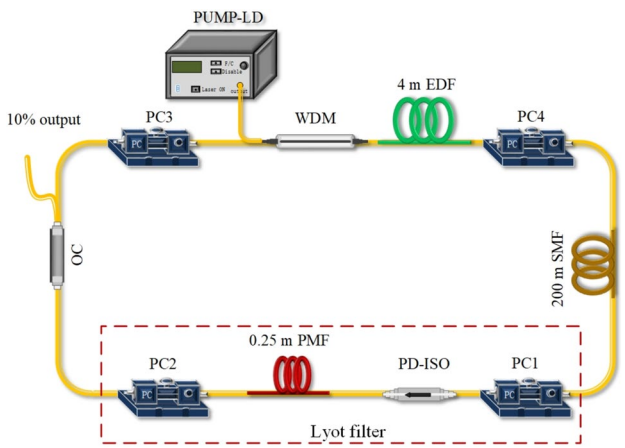

Fig. 1 Experimental setup of a ring PMLFL

NPR-based filtering effects shared a PD-ISO, resulting in these two filtering effects being coupled to form a composite filtering function. The entire cavity length was approximately 206.5 m, corresponding to a fundamental repetition rate of 1.016 MHz. The 10% terminal of a Y-type coupler was used as the output of the entire laser fiber. The net cavity dispersion was experimentally estimated to be – 3.93 ps^2 at 1565.6 nm based on the features of soliton Kelly sidebands, which indicate that the fiber laser operated in the anomalous group velocity dispersion region. The optical spectrum, autocorrelation trace, temporal response and radio-frequency (RF) of pulse signals were measured by an optical spectrum analyzer (OSA, Yokogawa AQ6375B), a frequency resolved optical grating measurer (FROG, Mesa Photonics), a 13-GHz oscilloscope (Lecroy, Wavemaster 813Zi-B) with a 12.5-GHz photoelectronic detector (EOT, ET–3500F) and a 3-GHz RF spectrum analyzer (Rigol DSA1030) with a 12.5-GHz photoelectronic detector (Newport, 818–BB–51F), respectively. The resolution of the OSA was kept at the highest precision of 0.01 nm during the measurement processes. It was noted that the signal should be amplified by an amplifier (Teraband LTRAN LOA3000) to reach sufficient power for the autocorrelation measurement based on second-harmonic generation before it was plugged into the FROG. The FROG could carry out two operations, i.e., the autocorrelation measurement and the reconstruction of the pulse profiles and phases, in which the wavelength-dependent intensity response differences were not considered during the measurement process.

NPR-based filtering can be expressed as [19]

$$T_{NPR} = \cos^2\alpha_1\cos^2\alpha_2 + \sin^2\alpha_1\sin^2\alpha_2 + \frac{1}{2}\sin 2\alpha_1\sin 2\alpha_2\cos\left(\Delta\varphi_l + \Delta\varphi_{nl}\right). \quad (1)$$

Here, α_1 and α_2 are the angles between the polarization directions of the PD-ISO on both sides and the fast axes of the SMF, respectively. Linear and nonlinear phase delays of mode-locked pulses are depicted as $\Delta\varphi_l = 2\pi L(n_x - n_y)/\lambda_0$ and $\Delta\varphi_{nl} = 2\pi n_2 PL\cos 2\alpha_1/\lambda_0 A_{\text{eff}}$. In addition, L, $n_x - n_y$, λ_0, n_2, P and A_{eff} are the main cavity length, refractive index difference of the two polarization axes of the SMF, operating wavelength, nonlinear refractive index coefficient, instantaneous power of the input signal and effective fiber core area, respectively. On the other hand, Lyot-based filtering can be expressed as [20]

$$T_{Lyot} = \frac{1}{2}cos^2\left(\frac{\pi\Delta n}{\lambda}L_{PMF}\right)(1 + sin2\theta), \quad (2)$$

where Δn, L_{PMF} and θ are the refractive index difference between the slow and fast axes of PMF, PMF length and the angle between the polarization direction of the input light and the fast axis of the PMF, respectively. According to Eqs.

(1) and (2), it is clear that NPR- and Lyot-based filtering functions vary periodically with wavelength. They can be regarded as comb filters, whose transmissivity peaks can support pulse generation in the cavity. In our experiments, these two filtering effects can be coupled to form a composite filtering function, assisted by the shared PD-ISO. Then, the transmissivity profile of the composite filtering effect dynamically adjusted by different multiplication operations between NPR- and Lyot-based filtering functions can be expressed as follows:

$$T_{composite} = T_{NPR} \cdot T_{Lyot}. \tag{3}$$

3 Experimental results

Single solitons self-started at a threshold pump power of 6 mW, and dual-wavelength solitons were further achieved at a pump power of 40 mW. Fixed at a pump power of 100 mW, the processes from the coexistence, incoherent interaction, and weakly coherent interaction of dual-wavelength pulses to the generation of an SM, as shown in Fig. 2, could be experimentally observed by dynamically adjusting PCs. We set 0° for holding blocks of all PCs at a horizontal position. We could rotate the angles of holding blocks of PCs clockwise for adjusting the polarization settings in the cavity. In particular, Fig. 2m shows a colormap of 1-h continuous spectral measurements at a 1-min interval for four operation regions. When the angles of the four PCs were simultaneously set at 30° (Region I of Fig. 2m), the transmissivity function of composite filtering composed of two principal transmissivity peaks with the same bandwidths of 2.5 nm centered at 1556.5 nm and 1566 nm (Fig. 2a) supported the coexistence of two discrete solitons with conventional Kelly sidebands (Fig. 2i). Due to the temporal spacing Δt between dual-wavelength solitons being beyond the direct measurement range of the FROG and the oscilloscope, we adopted the mathematical relationship between temporal and spectral information described in Ref. [19] to calculate Δt:

$$\Delta t = |D| \cdot L \cdot \Delta\lambda, \tag{4}$$

where $\Delta\lambda$ and D are the spectral interval of two solitons and the fiber dispersion coefficient, respectively. Then, Δt is 37.34 ps for the average dispersion coefficient of the cavity $D = -19.03$ ps/(km·nm), the spectral interval of two solitons $\Delta\lambda = 9.5$ nm and the cavity length $L = 206.5$ m. The pulse spacing is far beyond the maximum direct interaction distance of a five-time pulse duration. Thus, dual-wavelength solitons coexist in the fiber laser without any interaction. The dual-wavelength solitons have a good stability with a high signal-to-noise ratio (SNR) of 75 dB [left inset of Fig. 2e]. However, the oscilloscope and the autocorrelator cannot distinguish these two solitons due to the limit of the measurement accuracy. The autocorrelation trace, as shown in Fig. 2e, is characterized by a single peak structure with a 2.73-ps pulse width which is assumed as pulse widths of the two solitons. The 3-dB spectral widths of the two solitons are 1.2 nm and 1.13 nm at the central wavelengths of 1556.5 nm and 1566 nm, respectively, as depicted in Fig. 2i. The corresponding time-bandwidth products are calculated to be 0.41 and 0.38, respectively, indicating that the dual-wavelength solitons were nearly transform-limited pulses with slightly larger chirps. The electronic response of the pulses in the oscilloscope shows a single pulse train with a temporal spacing of 0.983 μs [right inset of Fig. 2e], corresponding to a fundamental repetition rate. When PC1 and PC2 were fixed at 30° and PC3 and PC4 were set at 45° [Region II of Fig. 2m], the composite filtering profile exhibited two adhered transmissivity peaks with a shorter spectral interval of 5 nm (Fig. 2b) to promote the closer proximity of the dual-wavelength pulses. A double-soliton superposition state without regular modulated ripples (Fig. 2j) was achieved except for a resonant spectral spike appearing in the overlapping region. Thus, Region II indicates that these solitons only had an incoherent interaction. The temporal characteristics of Region II in Fig. 2f are similar to those of

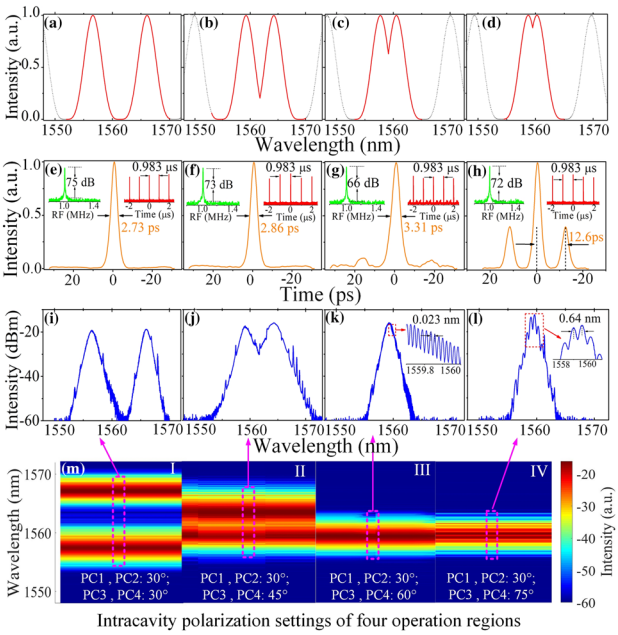

Fig. 2 Processes from the coexistence, incoherent interaction and weakly coherent interaction of dual-wavelength pulses to an SM. **a**–**d** Transmissivity curves of the composite filtering at four operation regions; **e**–**h** corresponding autocorrelation traces, left inset: RF, right inset: pulse train; **i**–**l** corresponding spectra; **m** spectral color maps of four operation regions

Region I in Fig. 2e, exhibiting a single-peaked autocorrelation trace with a 2.86-ps pulse width, a single pulse train with a spacing of 0.983 μs [right inset of Fig. 2f] and an SNR of 73 dB [left inset of Fig. 2f]. The intensity trend of the autocorrelation traces in Fig. 2e, f described by Pearson's correlation coefficient [21] is 99.96%, indicating that the two cases had almost identical structural similarity. However, the autocorrelation pedestal of Fig. 2f is slightly larger than that of Fig. 2e. The mean squared error between them is 0.32, indicating that the two cases still had evident intensity difference. Especially, the increase in the pedestal of Fig. 2f originated from split components induced by incoherent interaction between dual-wavelength solitons. When PC3 and PC4 were further adjusted toward 60° [Region III of Fig. 2m], the interval of the two transmissivity peaks further shortened to 2.8 nm (Fig. 2c). The coexistence of two independent pulses evolved into a weakly bound state with dense modulated ripples distributed across the spectrum (Fig. 2k). The interval between adjacent spectral ripples shown in the inset of Fig. 2k was 0.023 nm, corresponding to a temporal pulse spacing of 352.2 ps that was far beyond the measurement range of the FROG. The weakly bound state is characterized by a pair of small spikes distributed on both sides of the principal autocorrelation peak (Fig. 2g), a more pronounced background noise surrounding the pulse train [right inset of Fig. 2g] and a lower SNR of 66 dB [left inset of Fig. 2g]. The autocorrelation information of the pulse width broadened by 21% and the ratio between principle and secondary spikes of 1:0.1 indicated that two solitons dynamically varied in the bound unit due to the weak coherent interaction. Thus, the weakly bound state had less stability than the dual-wavelength soliton state. When the angles of PC3 and PC4 arrived at 75° [Region IV of Fig. 2m], two transmissivity peaks of the composite filtering reached the minimum spectral interval of 2 nm but still retained a similar profile (Fig. 2d). The strong trapping between two pulses resulted in the synthesis of an SM based on a coherent interaction, as shown in Fig. 2l. The SM had the intrinsic properties of periodic spectral fringes across the spectrum with a 0.64-nm interval [inset of Fig. 2l] and a pair of small spikes distributed on both sides of the principal spike in the autocorrelation trace with a 12.6-ps spacing (Fig. 2h). The mathematical relationship between the interval $\Delta\lambda$ of the spectral fringes and temporal spacing $\Delta\tau$ of internal pulses for an SM is described in Ref. [22]:

$$\Delta\tau = \left| \frac{{\lambda_0}^2}{c \cdot \Delta\lambda} \right|, \tag{5}$$

where c is the speed of light in a vacuum. The experimental results of the 0.64-nm interval of spectral fingers in Fig. 2l and the 12.6-ps spacing between autocorrelation spikes in Fig. 2h perfectly obeyed the mathematical relationship of Eq. (5). Moreover, the SM with less background noise [right inset of Fig. 2h] and a larger SNR of 72 dB [left inset of Fig. 2h] showed more stability than the weakly bound state in Region III. In summary, there is a rule for the SNR dependent on the interaction between two solitons in the synthesis process of an SM, i.e., the SNR first has a larger value for the case of no interaction between two solitons, then becomes smaller for the case of incoherent interaction, subsequently increases for the case of weak coherent interaction, and finally arrives at the initial level for the case of coherent interaction between internal pulses in an SM.

An iterative phase-retrieval algorithm can be used to invert the FROG trace of the measured pulse into the pulse profile and its phase in real time. Refs. [23, 24] demonstrated using a developed two-dimensional phase-retrieval algorithm called the principal components generalized projections algorithm for inverting FROG traces to display the intensity and phase of ultrashort pulses in a continuous manner at fast speeds. The operation mechanism of the phase-retrieval algorithm was to first introduce an initial phase for constructing an optical pulse field based on the experimentally achieved spectral data, and then to compare with the error of the similarity between the theoretically calculated autocorrelation trace and the experimental result. When the error arrived at a given target, the iterative calculation process would be terminated. To further understand the characteristics of SMs, Fig. 2h was used to theoretically invert the genuine pulse profiles and phases based on the FROG inversion algorithm. Figure 3 illustrates the SM profile inverted from the measured FROG trace in Fig. 2h. It is clear that the SM is composed of two solitons with a spacing of 12.6 ps. Both solitons had the same pulse duration of ~ 2.2 ps. Moreover, the two solitons had different intensities with a ratio of 1:0.3. The phase curve in pink reveals that the two internal solitons of the SM have a locked phase difference of –7.8, which is ~ –0.5π. The error of the inversion process was estimated to be ~ 0.0805 by the FROG. In general, internal solitons in a conventional SM showed uniform pulse intensity, as described in Ref. [8], due to the

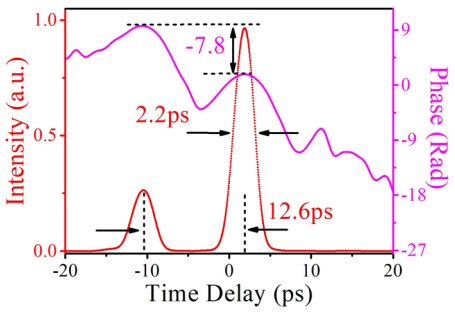

Fig. 3 Inverted SM at a pump power of 100 mW based on the FROG trace of Fig. 2h. Red: pulse profiles; pink: phases

soliton energy quantization effect, which caused an original pulse with a high energy level to self-split into two identical pulses. However, internal pulses of our synthesized SMs generated from different transmissivity peaks of composite filtering could have a strong gain competition in the same gain band. Thus, internal pulses of our SMs always exhibited nonuniform pulse intensity, which is a major difference from conventional SMs. On the other hand, the formation of SMs in Ref. [8] originated from the CW-induced local direct interaction. However, our synthesized SMs were due to filtering-induced coherent interaction.

To verify the validity of the synthesis technique demonstrated by Fig. 2, other SMs with different pulse spacings and phases would be experimentally synthesized further by changing the composite filtering profiles. The pump power was fixed at 20 mW, and the angles of PC1 and PC2 were set at 30° in the following experiments. Then, the adjustment of the composite filtering profiles could be carried out by dynamically adjusting PC3 and PC4. For example, when the angles of PC3 and PC4 were adjusted toward 65°, we achieved another new SM composed of two 2.5-ps solitons. This SM has the characterized properties of a modulated spectrum with periodic fringes with a 0.5-nm interval and a principal autocorrelation spike accompanied by a pair of symmetrical small spikes on both sides with a temporal spacing of 16.2 ps, as shown in Fig. 4a. The phase difference between two solitons inside the SM was locked at –1.57 (Fig. 4b), which was approximately –0.5π. The inverted temporal SM profile is also exhibited in Fig. 4b based on the FROG inversion algorithm. The SM had similar characteristics compared with the case of Fig. 2h except for a slightly larger pulse duration and spacing. Similarly, other new SMs composed of two solitons on the picosecond scale with pulse spacings of 16.8 ps (Fig. 4c) and 23.8 ps (Fig. 4e) were experimentally synthesized when the angles of PC3 and PC4 were further adjusted toward 70° and 75°, respectively. The corresponding inverted phase differences were estimated to be –9.4 (~–π) (Fig. 4d) and –4.7 (~–0.5π) (Fig. 4f), respectively. These synthesized SMs had the same characteristics as the SMs with phases of –π and –0.5π in Ref. [25]. In summary, the experimental synthesis of SMs with different pulse spacings, wavelength intervals and phases can be dynamically achieved by adjusting the composite filtering functions. The wavelength intervals of two solitons in SMs are decided by the spectral interval of the two principal transmission peaks of composite filtering functions.

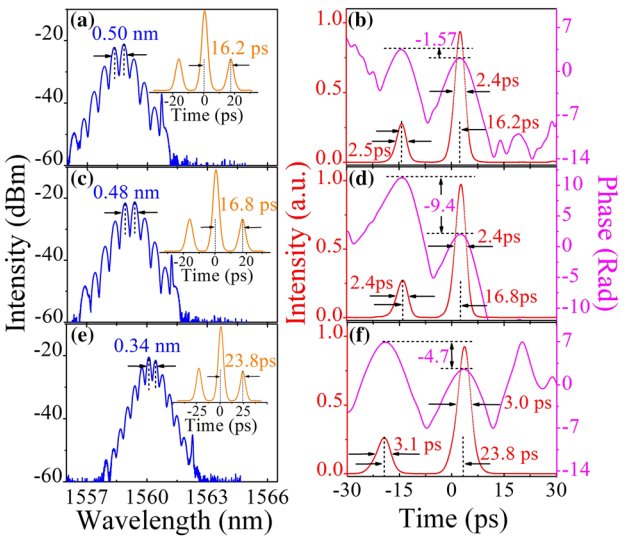

Fig. 4 Characteristics of SMs with a pump power of 20 mW. **a**, **c**, **e** Spectra (inset: autocorrelation traces); **b**, **d**, **f** inverted SMs (red: pulse profiles; pink: phases)

4 Theoretical analysis and simulation

To reproduce the buildup process of SMs, the simulations for the laser setup model in Fig. 1 are performed in accordance with the experimental conditions. The transient process from white noise to an SM state is theoretically calculated using the ray-tracing method. That is, the optical field is multiplied by a corresponding transmission matrix when it passes through an optical device. The propagation of the laser slow-varying envelope amplitude u in the EDF can be described through the Ginzburg–Landau equation [26]:

$$\frac{\partial u}{\partial z} = -i\frac{\beta_2}{2}\frac{\partial^2 u}{\partial t^2} + i\gamma|u|^2 u + \frac{g}{2}u + \frac{g}{2\Omega^2}\frac{\partial^2 u}{\partial t^2}, \tag{6}$$

where β_2, g and Ω are the group velocity dispersion, saturation gain and gain bandwidth of the EDF, respectively. It is notable that Eq. (6) is numerically calculated by the split-step Fourier method. In addition, the saturation gain intensity is expressed as follows:

$$g = g_0 exp\left(-\frac{\int |u|^2 dt}{Es}\right), \tag{7}$$

where g_0 and Es are the small signal gain coefficient and gain saturation energy, respectively. When the signal propagates in the SMF, g is set to zero, leading to Eq. (6) becoming a typical nonlinear Schrödinger equation. For simplification, the NPR-induced artificial saturation absorption T_{sat} is expressed as [27]

$$T_{sat} = 1 - \frac{m_0}{\left[1 + \frac{P(t)}{P_{sat}}\right]}, \tag{8}$$

where m_0, $P(t)$ and P_{sat} are the unsaturated loss, instantaneous pulse power and saturation power, respectively.

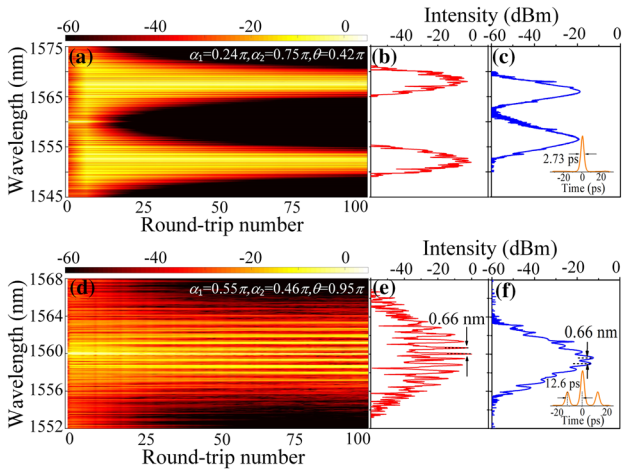

Fig. 5 Simulation for the experimental cases of dual-wavelength solitons and an SM. **a** Buildup process of dual-wavelength solitons. **b** Output spectrum at the 100th round-trip. **c** Experimental spectrum of (**b**), inset: autocorrelation trace. **d** Buildup process of an SM. **e** Output spectrum at the 100th round-trip. **f** Experimental spectrum of (**e**), inset: autocorrelation trace

In the simulation, the propagation of the optical field in the EDF and SMF described by Eq. (6) is first calculated using white noise as the initial signal and then successively multiplied by an NPR-induced saturable absorption function T_{sat} described by Eq. (8) and a composite filtering function described by Eq. (3). The 90% output from the OC is used as the initial input for the next cycle in the laser. The calculations are carried out repeatedly until the optical field arrives at a self-consistent state.

According to the experimental conditions, the simulation parameters are selected as follows: $\beta_{2,\,SMF}=-20$ ps^2/km, $\gamma_{SMF}=2$ W^{-1} km^{-1}, $\beta_{2,\,EDF}=65$ ps^2/km, $\gamma_{EDF}=4.2$ W^{-1} km^{-1}, $g_0=1$ dB/m, $\Omega=15$ nm, $m_0=0.1$, $L_{PMF}=0.25$ m, $L_{EDF}=4$ m, $L_{SMF}=203$ m and $P_{sat}=50$ W. When α_1, α_2 and θ are set to 0.24π, 0.75π and 0.42π, respectively, which is equivalent to the simultaneous adjustment of the NPR- and Lyot-based filtering profiles to form the composite filtering described in Fig. 2a, a transient buildup process from white noise to a dual-wavelength soliton state is simulated to show in Fig. 5a. The white noise is reshaped into two discrete pulses in the fiber laser after the 12th round-trip. Then, stable dual-wavelength solitons are further obtained after the 60th round-trip. However, these solitons independently evolve without any interaction during propagation. The experimentally achieved spectrum of dual-wavelength solitons under the abovementioned conditions, as shown in Fig. 5c, has a similar property of two separated bell-shaped profiles compared with the calculated spectrum at the 100th round-trip in Fig. 5b. The experimental autocorrelation trace, the inset of Fig. 5c, exhibits a spike due to the limit of measurement accuracy. Subsequently, when α_1, α_2 and θ are set to 0.55π, 0.46π and 0.95π, respectively, i.e., adjusting NPR- and Lyot-based filtering functions to construct another composite filtering described in Fig. 2d, the transient buildup process from white noise to an SM state is shown in Fig. 5d. White noise directly reshapes into a bound state at the initial stage from 0 to the 25th round-trip and eventually into an SM after the 45th round-trip. The calculated spectrum of a stable SM at the 100th round-trip is achieved, as shown in Fig. 5e, by possessing an inherent property of spectral fringes with an interval of 0.66 nm across the spectrum (corresponding to a spacing of 12.6 ps), which is in agreement with the experimental results in Fig. 5f. The experimentally achieved SM spectrum with weak fringes is maybe due to that the average measurement of the OSA lowers modulated depths. It is notable that other physical effects remain unchanged except that the composite filtering is adjusted in the simulation. Thus, composite filtering is beneficial for the manipulation of SM generation.

5 Conclusion

In conclusion, we manipulate the interaction of dual-wavelength pulses for synthesizing SMs with different pulse spacings and phases by constructing composite filtering functions in a fiber laser. Theoretical and experimental analyses demonstrate that the composite filtering functions can be used to synthesize different SMs. Our work will provide a novel coherent pulse synthesis technique in the fields of pulse coding and coherent pulse detection.

Acknowledgements This work was supported in part by the Project of Department of Education of Guangdong Province under Grant No. 2021ZDJS105, in part by the National Natural Science Foundation of China under Grant Nos. 62375053 and 61875242, and in part by the Research Fund of Department of Science and Technology of Guangdong Province under Grant Nos. 2020B1212030010 and 2020B1212060067.

Author contributions Lin Gu and Zhen Liu wrote the manuscript. Yiqing Shu, Jianqing Li and Weicheng Chen provided conceptualization, methodology and supervision.

Data availability Data will be made available on request.

Declarations

Conflict of interest The authors declare that they have no known competing financial interests or personal relationships that could have appeared to influence the work reported in this paper.

References

1. J. Zeng, M.Y. Sander, Opt. Lett. **45**, 5 (2020)
2. Y. He, M. Li, Y. Shu, Q. Ning, W. Chen, A. Luo, Opt. Fiber Technol. **61**, 102453 (2021)

3. W.-C. Chen, G.-J. Chen, D.-A. Han, B. Li, Opt. Fiber Technol. **20**, 199 (2014)
4. J. Peng, H. Zeng, Commun. Phys. **2**, 34 (2019)
5. L. Gui, P. Wang, Y. Ding, K. Zhao, C. Bao, X. Xiao, C. Yang, Appl. Sci. **8**, 201 (2018)
6. G. Herink, F. Kurtz, B. Jalali, D.R. Solli, C. Ropers, Science **356**, 50 (2017)
7. B.A. Malomed, Phys. Rev. A **44**, 6954 (1991)
8. D.Y. Tang, W.S. Man, H.Y. Tam, P.D. Drummond, Phys. Rev. A **64**, 033814 (2001)
9. B. Liu, Y. Liu, Y. Luo, Y. Xiang, P.P. Shum, X. Tang, D. Liu, Q. Sun, Opt. Commun. **457**, 124700 (2020)
10. M. Stratmann, T. Pagel, F. Mitschke, Phys. Rev. Lett. **95**, 143902 (2005)
11. W.C. Chen, Z.C. Luo, W.C. Xu, Laser Phys. Lett. **6**, 816 (2009)
12. P. Ryczkowski, M. Närhi, C. Billet, J.-M. Merolla, G. Genty, J.M. Dudley, Nat. Photonics **12**, 221 (2018)
13. Z. Chang, L. Kong, Y. Cao, A. Liu, Z. Li, Q. Wu, J. Huang, L. Gao, T. Zhu, Opt. Laser Technol. **149**, 107859 (2022)
14. C. Li, J. He, Y. Liu, Y. Yue, L. Zhang, L. Zhu, M. Zhou, C. Liu, K. Zhu, Z. Wang, Photonics **8**, 51 (2021)
15. R. Hao, L. Li, Z. Li, W. Xue, G. Zhou, Opt. Commun. **236**, 79 (2004)
16. W. He, M. Pang, D.-H. Yeh, J. Huang, P.S.J. Russell, Light Sci. Appl. **10**, 120 (2021)
17. L. Nimmesgern, C. Beckh, H. Kempf, A. Leitenstorfer, G. Herink, Optica **8**, 1334 (2021)
18. S. Liu, Y. Cui, E. Karimi, B.A. Malomed, Optica **9**, 240 (2022)
19. R.H. Stolen, J. Botineau, A. Ashkin, Opt. Lett. **7**, 512 (1982)
20. B. Lyot, C.R. Acad, Sci. **197**, 1593 (1933)
21. K. Pearson, Philos. T. R. Soc. A **185**, 71–110 (1894)
22. C. Wang, L. Wang, X. Li, W. Luo, T. Feng, Y. Zhang, P. Guo, Y. Ge, Nanotechnology **30**, 025204 (2018)
23. D.J. Kane, J. Opt. Soc. Am. B **25**, 120 (2008)
24. D.J. Kane, IEEE J. Quantum Electron. **35**, 421 (1999)
25. L. Gui, X. Xiao, C. Yang, J. Opt. Soc. Am. B **30**, 158 (2013)
26. V.L. Ginzburg, L.D. Landau, Zh. Eksp, Teor. Fiz. **20**, 1064 (1950)
27. M. Li, Y. Shu, L. Gu, Z. Cui, A. Luo, Y. Li, W. Chen, Opt. Laser Technol. **145**, 107480 (2022)